CrossMark

Extremely Relativistic Tidal Disruption Events

Taeho Ryu[1,2] , Julian Krolik[2] , and Tsvi Piran[3]
[1] The Max Planck Institute for Astrophysics, Karl-Schwarzschild-Str. 1, Garching, D-85748, Germany; tryu@mpa-garching.mpg.de
[2] Physics and Astronomy Department, Johns Hopkins University, Baltimore, MD 21218, USA
[3] Racah Institute of Physics, Hebrew University, Jerusalem 91904, Israel
Received 2022 October 31; revised 2023 March 9; accepted 2023 March 10; published 2023 March 29

Abstract

Extreme tidal disruption events (eTDEs), which occur when a star passes very close to a supermassive black hole, may provide a way to observe a long-sought general relativistic effect: orbits that wind several times around a black hole and then leave. Through general relativistic hydrodynamics simulations, we show that such eTDEs are easily distinguished from most tidal disruptions, in which stars come close, but not so close, to the black hole. Following the stellar orbit, the debris is initially distributed in a crescent, it then turns into a set of tight spirals circling the black hole, which merge into a shell expanding radially outwards. Some mass later falls back toward the black hole, while the remainder is ejected. Internal shocks within the infalling debris power the observed emission. The resulting lightcurve rises rapidly to roughly the Eddington luminosity, maintains this level for between a few weeks and a year (depending on both the stellar mass and the black hole mass), and then drops. Most of its power is in thermal X-rays at a temperature $\sim(1$–$2) \times 10^6$ K (~100–200 eV). The debris evolution and observational features of eTDEs are qualitatively different from ordinary TDEs, making eTDEs a new type of TDE. Although eTDEs are relatively rare for lower-mass black holes, most tidal disruptions around higher-mass black holes are extreme. Their detection offers a view of an exotic relativistic phenomenon previously inaccessible.

Unified Astronomy Thesaurus concepts: Tidal disruption (1696); Supermassive black holes (1663); Hydro-dynamics (1963); General relativity (641); Gravitation (661)

1. Introduction

Almost every galaxy harbors a supermassive black hole (SMBH) at its center (Kormendy & Ho 2013). Well before observational data established this fact, theoretical work (e.g., Lacy et al. 1982; Carter & Luminet 1983; Rees 1988) demonstrated that if a star approaches an SMBH closer than a "tidal radius" that is $\sim\Psi(M_\star, M_{\rm BH})(R_\star(M_{\rm BH}/M_\star)^{1/3}$ (here $M_{\rm BH}$ and $M_\star$ are the mass of the black hole (BH) and the star, respectively, $R_\star$ is the stellar radius, and $\Psi(M_\star, M_{\rm BH})$ is a correction factor of order unity; Ryu et al. 2020a), it is disrupted by the SMBH's tidal gravity. For $M_{\rm BH} = 10^6 M_\odot$, the critical distance for total disruption of main-sequence stars is $\simeq 25 r_{\rm g}$ ($r_{\rm g} \equiv GM_{\rm BH}/c^2$), nearly independent of $M_\star$ (Ryu et al. 2020a). In ordinary TDEs, those in which the star's pericenter $r_{\rm p}$ is not far inside the critical radius, the star follows an essentially parabolic orbit as it approaches the SMBH. After the disruption, the debris forms an elongated structure. Half the matter is unbound and rushes away, while the other half is placed on highly eccentric ($1 - e \sim 2(M_{\rm BH}/M_\star)^{-1/3}$) orbits (see the lower panels of Figure 1). Near their apocenters, the orbits of different streams of bound matter intersect, dissipating energy with a rest-mass efficiency $\sim10^{-4}$–10^{-3}. The result of these interactions is an irregular, crudely elliptical accretion flow (e.g., Piran et al. 2015; Shiokawa et al. 2015; Svirski et al. 2017; Steinberg & Stone 2022).

In the last $\simeq 15$ yr, roughly 100 such events have been observed (Gezari 2021), generally producing an optical/UV luminosity similar to what the stream intersections would yield (Piran et al. 2015). The luminosity of such a flare grows on the timescale of the orbital period of the most-bound debris, $t_0 \sim 1$ month $(M_{\rm BH}/10^6 M_\odot)^{1/2}(M_\star/M_\odot)^{-1}(R_\star/R_\odot)^{3/2}\Xi(M_\star, M_{\rm BH})^{-3/2}$ month

(Rees 1988), where Ξ is an order-unity correction (Ryu et al. 2020a). After the peak is reached, the rate at which bound mass returns to the neighborhood of the SMBH declines $\propto t^{-5/3}$ (Rees 1988; Phinney 1989), and many (but by no means all) observed TDE lightcurves follow this trend (Komossa & Bade 1999; Halpern et al. 2004; Hung et al. 2017; van Velzen et al. 2021).

Remarkably, even though an SMBH causes the tidal disruption, in ordinary TDEs much of the subsequent evolution of the debris can be explored using Newtonian dynamics. However, general relativity changes the character of orbits dramatically when their pericenter distance is $<6r_{\rm g}$. When a star falls from far away with a total energy very close to its rest-mass energy and passes this close to an SMBH, rather than tracing a parabola as it would under Newtonian gravity, relativistic apsidal precession is so strong that the pericenter region wraps all the way around the SMBH (Figure 2). In extreme cases, the orbit can go several times around the SMBH while keeping a distance just slightly greater than the pericenter. Only after completing these circuits can the orbital path once again extend out to large distance. When a star follows such an orbit, the time during which it suffers extremely strong tidal gravity can be is greatly extended, an effect that, as we will show here, dramatically alters the fate of its postdisruption debris.

Several earlier works investigated the initial stage of stream evolution in such extreme disruptions. Laguna et al. (1993) were the first to simulate eTDEs, considering a case with $r_{\rm p} = 4.7 r_{\rm g}$. Kobayashi et al. (2004) reconsidered the same event focusing on the gravitational wave signature during the strongest compression of debris at the first pericenter passage. Later, eTDEs have been simulated to examine the impact of relativity on the energy and angular momentum distributions of the debris immediately after it leaves the star
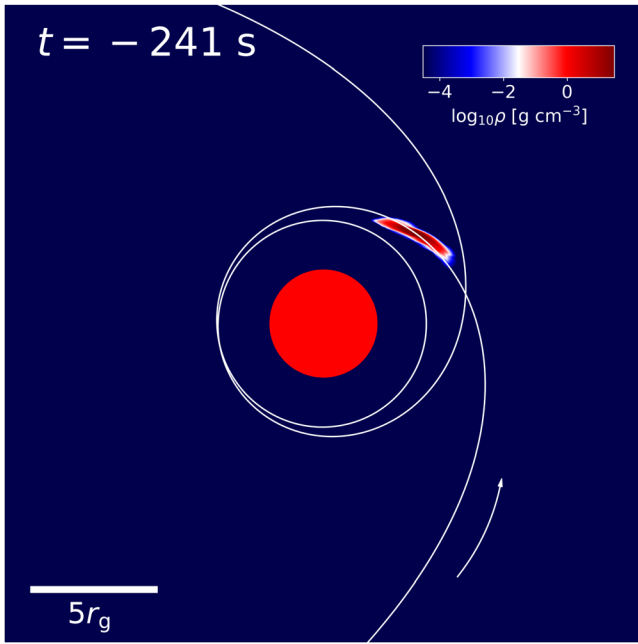
Figure 2. The solid white curve depicts the geodesic of an orbit with $r_p \simeq 4.03 r_g$ around an SMBH (red disk at the center); the arrow indicates the direction of the orbit. The color scale shows the density distribution of stellar debris 241 s before a star whose center of mass follows this geodesic passes through pericenter.

(e.g., Cheng & Bogdanović 2014) and to compare the initial stage of stream evolution in nonspinning and spinning SMBHs (e.g., Tejeda et al. 2017; Gafton & Rosswog 2019). All these previous studies found that immediately after disruption the debris forms a crescent around the SMBH; those running a little bit longer found that the crescent becomes a spiral. However, all stopped when the debris was still close to the SMBH.

Other studies considered stars on orbits with pericenters $7r_g \leqslant r_p \leqslant 20r_g$ passing by a BH with mass $\sim 10^5 M_\odot$ (e.g., Evans et al. 2015; Darbha et al. 2019). In these cases, a small part of the star came close to the BH, but the majority was too far away to reveal the effects we discuss here. In fact, the debris in these simulations does not form a crescent; instead it resembles the common TDE debris structure.

Here, we report on the first simulations that follow the evolution of the debris from an eTDE long enough to estimate the observational signature. Our simulations, which are fully relativistic, continue far beyond the longest endpoint of previous work. We find that at later times the debris undergoes multiple shape transitions, which ultimately lead to formation of a hot accretion flow near the SMBH (see Figure 2). This inner hot flow is the main source powering the event's flare, whose observational signature, both lightcurve and spectrum, are very different from those observed in ordinary TDEs.

Our paper is organized as follows: we begin with a detailed description of the numerical methods in Section 2. Our results are presented in Section 3, and their implications are discussed in Section 4. We summarize and conclude in Section 5.

2. Numerical Methods

We performed a series of fully relativistic hydrodynamics simulations of tidal disruptions of a realistic star on very deeply plunging zero binding-energy orbits around a $10^6 M_\odot$ SMBH, using the grid-based code HARM3D (Noble et al. 2009). As described in Ryu et al. (2020b), the initial state of all the stars was taken from a stellar model for a $1 M_\odot$ middle-aged main-sequence star evolved using the stellar evolution code MESA (Paxton et al. 2011).

The first stage of our calculations uses the Ryu et al. (2020b) method, in which the star's dynamics are computed in a Cartesian domain that extends $5R_\star$ in each dimension and follows the star's center of mass along its geodesic until the star is completely disrupted. In this approach, the star's self-gravity is calculated with the Newtonian Poisson equation in an orthonormal tetrad frame comoving with the star. Because the metric in this frame departs from Minkowski by very small amounts within the simulation domain, the potential can be added as a perturbation to g_{tt}. The modified tetrad-frame metric is then transformed back to the simulation coordinates. This procedure ensures that the self-gravity calculations are consistent with relativity. Although the star becomes strongly distorted during this stage, negligible mass is lost from the box.

The second stage of the calculation begins when the tidal force completely dominates the self-gravity (at $r \lesssim 5$–$6r_g$). At this point, the tidal force is more than 1 order of magnitude greater than the self-gravity even a single cell away from the debris' center of mass. We therefore switch off the self-gravity, interpolate data from the box's Cartesian grid into the spherical grid, and continue to follow the evolution of the debris on a spherical grid that covers the entire volume near the SMBH (for details, see Appendix A). Self-gravity remains unimportant even in the long-term evolution of the debris because multiple shocks due to stream–stream collisions keep almost the entire debris hot.

Until the tidal force becomes dominant over the star's self-gravity, we evolve the gas using the equation of state $p = (\Gamma - 1)u$ with $\Gamma = 5/3$ where p is the pressure and u internal energy. When stellar self-gravity becomes negligible, we switch to an equation of state with an "effective adiabatic index" (Shiokawa et al. 2015) expressed as

$$\Gamma = \frac{4 + 5u_{gas}/u_{rad}}{3(1 + u_{gas}/u_{rad})}. \tag{1}$$

This form includes radiation pressure under the assumption of thermodynamic equilibrium. Here, u_{gas}/u_{rad} is the ratio of the gas internal energy density to the radiation energy density.

3. Results

Comparing the evolution of debris with four different values of $r_p = 4.03$, 5, 6 and $7r_g$ ($L \simeq 4.0 - 4.5 r_g c$), we find that extreme apsidal precession for $r_p < 6r_g$ (precession angle $> \pi/2$) causes debris evolution qualitatively different from ordinary disruption events that take place at larger r_p. The essential element is an orbit that stays very close to the SMBH for at least one complete circuit. Although in the following we describe in detail the results for $r_p \simeq 4.03 r_g$, debris behavior for orbits with $r_p \lesssim 6r_g$ is qualitatively similar. In sharp contrast, orbits with $r_p \simeq 7r_g$ produce debris flows akin to ordinary TDEs.

3.1. Overview of Dynamics

Figure 2 depicts the geodesic trajectory of the center of mass as well as the debris just before reaching the pericenter. As shown in this figure, the star makes two complete trips around the SMBH, maintaining a separation $\lesssim 4.1 r_g$ for nearly the
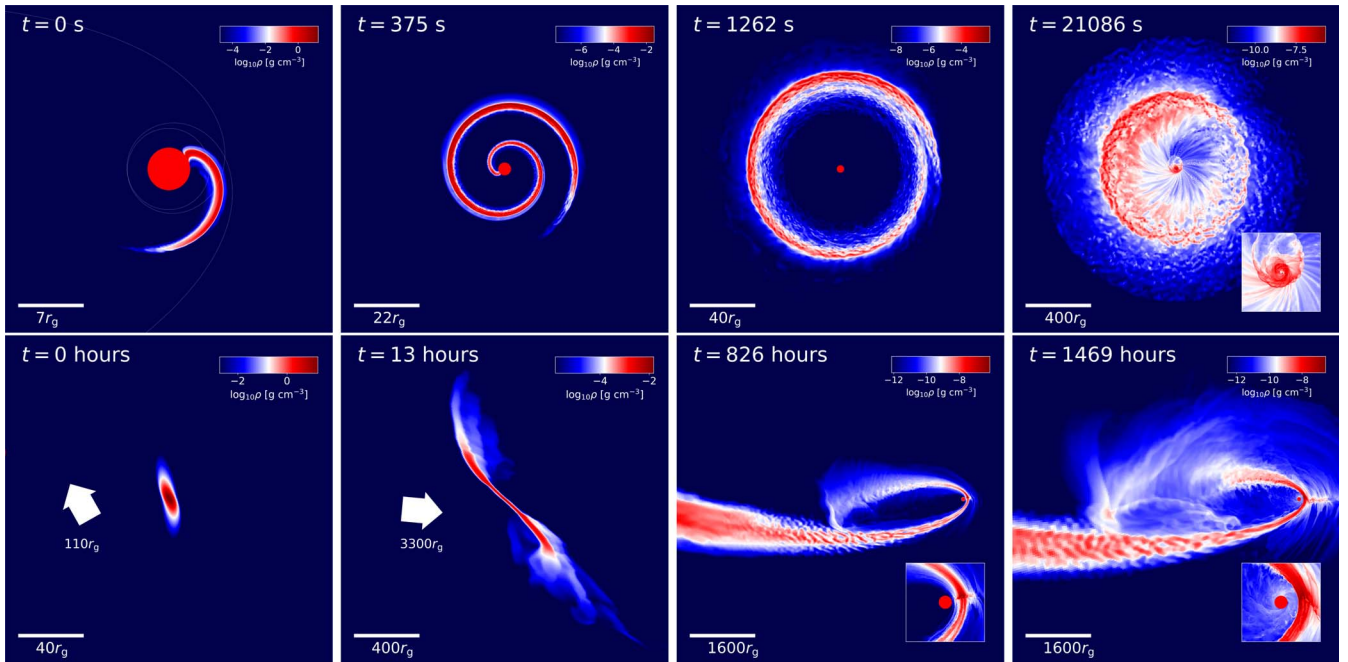
Figure 1. Illustration of the evolution and shape of debris in an extremely relativistic event with $r_p \sim 4.02 r_g$ (upper panels) and an ordinary TDE with $r_p \sim 110 r_g$ (lower panels). Four phases are shown for each. For the eTDE: crescent (note that the star has already been fully disrupted at this stage and a significant fraction of its mass has been captured); spiral; ring; and ring with inflow. For evolution of an ordinary TDE: beginning of the disruption; highly stretched star; and two stages of the stream's return to the vicinity of the SMBH. In all cases, the color scale represents the logarithmic density in the orbital plane. Insets show the matter near the SMBH.

entire time. While it does so, it continually loses mass; because of the strong apsidal precession, it spends enough time very close to the SMBH before reaching pericenter that it is wholly disrupted before the original stellar trajectory would reach the pericenter. Roughly 3/4 of the bound mass, close to half the star's initial mass, is captured immediately, some of it even before the nominal pericenter passage. Meanwhile, the remainder of the debris expands away from the star. As shown in the second upper panel of Figure 1, the result is a spiral of gas around the SMBH comprising both bound and unbound gas, but predominantly the latter. As the spiral expands further, its arms merge into a hot circular ring shown in the third upper panel; strong shocks accompany this merger. This ring then continues to expand. Ultimately (fourth upper panel), the bound matter in the ring falls back as it reaches its orbital apocenter at $\simeq 200 r_g$, shocking upon itself as it converges toward the SMBH. This last stage occurs (in our fiducial simulation) at $\sim 10^4$ s after the star is disrupted. Meanwhile, the unbound matter continues to move outward.

This behavior stands in a dramatic contrast to that of ordinary TDEs, in which the debris forms a long, narrow stream (see the first and second lower panels of Figure 1), and essentially all the bound mass is placed on highly elliptical orbits with apocenters several thousand r_g in size (Figure 1, third and fourth lower panels[4]), and dissipative events within this bound debris power the photon flare.

Importantly, the gas heating that powers the flare in eTDEs has a very different character from the stream–stream interactions seen in ordinary TDEs (e.g., Shiokawa et al. 2015). In eTDEs, shocks first form when the spirals merge into a shell, and then stronger shocks take place in the radially

infalling matter surrounding the SMBH. However, as illustrated in the fourth lower panel of Figure 1, in ordinary TDEs, shocks occur at specific intersection points between bound material moving on elliptical orbits, whether at a "nozzle shock" stretching along a line whose inner end is at $\simeq r_p$ (Shiokawa et al. 2015; Steinberg & Stone 2022) or at "apocenter shocks" taking place at a distance $\sim 100 \times$ that of the infall shocks in eTDEs. The shocks seen in eTDEs are also different from the discrete and isolated stream intersections envisioned as taking place when $r_p \lesssim 15 r_g$ (Lu & Bonnerot 2020; Batra et al. 2021).

3.2. Energetics

In an ordinary TDE, the distribution dM/dE of debris mass with orbital energy $E \equiv -(u_t + 1)$ is roughly a square wave with edges at $\Delta E = \pm \Xi \Delta \epsilon$, where $\Delta \epsilon = G M_{BH}^{1/3} M_*^{2/3} / R_*$, (Rees 1988) and $\Xi \approx 1$–2 (Ryu et al. 2020a). The top panel of Figure 3 displays both how different the immediately postdisruption dM/dE is from that of an ordinary TDE and how much it is redistributed well after the gas leaves the star. It also reveals how much of the bound debris is rapidly lost to accretion.

In an ordinary TDE, dM/dE is symmetric around $E = 0$, nearly flat from $E = -\Delta E$ to $E = +\Delta E$, and drops sharply for $|E| > \Delta E$ (Lodato et al. 2009; Guillochon & Ramirez-Ruiz 2013; Goicovic et al. 2019; Ryu et al. 2020b). In an eTDE, by $t \sim 230$ s after pericenter passage, although the energy distribution (in our fiducial simulation) is roughly symmetric, it is centered at $\simeq +(1$–2$)\Delta \epsilon$, and its half-width $\Delta E \sim 10 \, \Delta \epsilon$. The debris energy distribution found by Gafton & Rosswog (2019) at a similar time was qualitatively similar, but quantitatively different: narrower by a factor of a few and symmetric around $E \simeq 0$. This contrast may result from our use

---

[4] Data in the lower panels are taken from a simulation in which a $3 M_\odot$ middle-aged main-sequence star on a parabolic orbit with $r_p \simeq 110 r_g$ is disrupted by a $10^5 M_\odot$ SMBH (T. Ryu et al. in preparation).
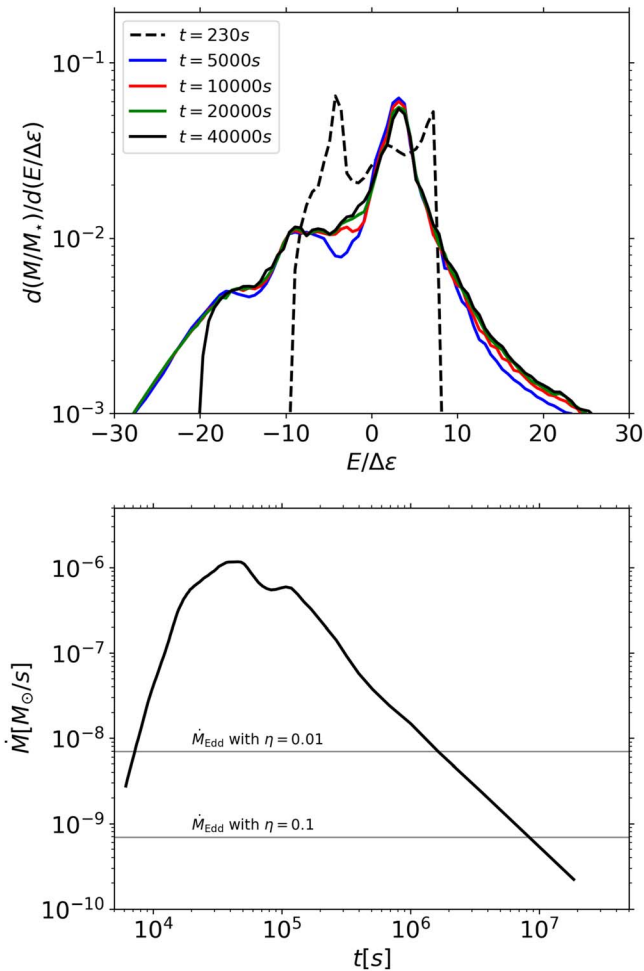
Figure 3. (Upper panel) The orbital energy distribution of the debris from a $1M_\odot$ star disrupted after following an orbit with $r_\mathrm{p} \simeq 4.03 r_\mathrm{g}$ around an SMBH with $M_\mathrm{BH} = 10^6 M_\odot$. Energy is in units of $\Delta\epsilon$. The black dashed line shows the energy distribution in the gas remaining immediately after half the stellar mass plunges directly into the SMBH; the four colored curves show its evolution at later times. Here, $E = -(1 + u_\mathrm{t})$ and $\Delta\epsilon = GM_\mathrm{BH}R_\star/r_\mathrm{t}^2$ where $r_\mathrm{t} = (M_\mathrm{BH}/M_\star)^{1/3}R_\star$. The time (in seconds) is measured since the initial pericenter passage. (Bottom panel) The thick black curve shows the mass fallback rate predicted from the energy distribution as of $t = 40,000$ s. The thin gray lines indicate the Eddington accretion rate assuming radiation efficiencies of $\eta = 0.01$ or 0.1.

of a main-sequence internal density profile rather than their $\gamma = 5/3$ polytrope.

However, this distribution soon changes drastically, a change not seen in previous work because their calculations stopped before it begins. Within ~ 10 minutes, most of the bound material plunges into the SMBH. By ~ 3 hr, the radial pressure gradient within the spirals broadens the distribution of the remaining matter by a further factor ~ 2–3, while also making it highly asymmetric and decidedly not flat-topped (see Figure 3, upper panel).

After the redistribution of energy, some of the bound material that had moved outward falls back toward the SMBH. The converging streams shock against each other, transforming orbital energy into heat. There it forms a compact ($\lesssim 100\,r_\mathrm{g}$), hot (a few 10^6 K), roughly spherical structure which is illustrated in the inset in the fourth panel of Figure 1. The most tightly-bound matter enters this structure first; the sharp low-energy cutoff in dM/dE at $t = 40,000$ s signals that the gas whose orbital energy had been $\simeq -(20$–$30)\Delta\epsilon$ has moved to

much more negative orbital energy due to dissipation in shocks. Unlike a classic Keplerian accretion disk that is supported by angular momentum, this accretion flow is geometrically thick and primarily radiation pressure supported: the mean specific angular momentum is only about half what would be required for a circular orbit in this range of radii.

Another consequence of the broad and asymmetric debris energy distribution is that the rate at which bound matter falls back toward the SMBH has a different time dependence from that of ordinary TDEs. Because dM/dE rises with increasing E steadily, but unevenly, across the entire range of bound energies, the postpeak decay of the mass fallback rate declines more slowly (see bottom panel of Figure 3) than in the case of ordinary TDEs—crudely $\propto t^{-5/4}$ rather than $\propto t^{-5/3}$. However, as we discuss in Section 4.1, as for ordinary TDEs (but for different reasons), the mass fallback rate does not translate directly into a lightcurve.

The unbound ejecta are contained in an axisymmetric ring of mass $\simeq 0.4 M_\odot$ that moves continuously outward once it forms. It simultaneously expands vertically as radiation forces compete with gravity. The distribution of outgoing speed at infinity can be estimated from the dM/dE distribution (Figure 3). For our fiducial case, the bulk of the unbound ejecta has specific orbital energy $\simeq (3$–$4)\Delta\epsilon$, corresponding to a speed $\simeq 9000$ km s^{-1} at infinity. The total kinetic energy available for deposition in the surrounding gas is $\simeq 10^{51}$ erg. However, a bit less than 1% of the ejecta mass has a speed $\gtrsim 21,000$ km s^{-1} at infinity, a factor of 3–4 faster than the same mass ejecta mass fraction for ordinary TDEs (Ryu et al. 2020a). This fast expanding debris that carries $\sim 10^{50}$ erg can produce a strong flare, as discussed in Section 4.3 below.

4. Observational Implications

4.1. Luminosity and Spectrum

The inner hot accretion flow is the main source of the radiation. We estimate the bolometric luminosity by integrating the local emissivity of cells within the photosphere whose cooling time is shorter than the evolution time. So that the surface brightness may be used to define a characteristic spectral temperature, we use the thermalization photosphere, defined as the location at $\sqrt{\tau_\mathrm{T}\tau_\mathrm{ff}} \simeq 1$, where τ_T is the Thomson optical depth and τ_ff the absorption optical depth, both of which are integrated over polar angle. See Appendix B for details.

The luminosity rises very rapidly—on a timescale of a few hours for the parameters of our simulations, rather than the ~ 1 month of ordinary TDEs,—and persists at roughly the Eddington luminosity (~ 2–3×10^{44} erg s^{-1} for $M_\mathrm{BH} = 10^6 M_\odot$) until at least $\sim 1/2$ day, the time at the end of our simulations. The speed of the lightcurve's rise can be seen in Appendix B, which illustrates how rapidly the volume of the cooling region within the observed photosphere grows at the beginning of an event.[5] At later times, the luminosity should persist at this level until the mass fallback rate becomes too small to support such a luminosity. At that point, it should decline with the shallow power law of the fallback rate. Our cooling time-based lightcurve estimate should capture the majority of the luminosity (the portion coming from the innermost region) reasonably well. The luminosity from the outer regions, whose cooling time is the longest, is more uncertain. Our method

---

[5] Note that for this purpose, we define the photosphere by integrating the effective opacity along radial paths of differing polar angle.

tends to overestimate it, but, because it is already a minority contributor, this means the actual luminosity may be less than estimated, but not by much. Future time-dependent transfer studies will clarify this situation.

To characterize the spectrum, we calculate the effective temperature for each surface element of the photosphere using the local area and the local luminosity. We find that the effective temperature distribution is well described by a single peak at $\sim 10^6$ K. Thus, the power is primarily in soft X-rays. For events driven by SMBHs of different masses, the luminosity peak should scale like the Eddington luminosity, $\propto M_{\rm BH}$, while the temperature is $\propto M_{\rm BH}^{-1/4}$ and the duration is $\propto M_* M_{\rm BH}^{-1}$. This last scaling follows from the fact that the emitted energy is $\propto M_\star$ (see next subsection), but nearly independent of $M_{\rm BH}$, while the Eddington luminosity is $\propto M_{\rm BH}$.

Although the peak luminosity is comparable to Eddington, there is relatively little matter far from the flow; consequently, reprocessing should be minor. To demonstrate this, in Appendix B we show the shape of the thermalization photosphere as seen by distant observers at several times; we define the photosphere by integrating the opacity inward from the outer boundary along radial paths. It is roughly axisymmetric everywhere; it is nearly flat close to the BH, e.g., at a distance $\simeq 100 r_{\rm g}$ from the equatorial plane for all radii $\gtrsim 100 r_{\rm g}$ at $t = 40{,}000$ s. As a result, the character of the continuum spectrum is determined fairly close to the site of initial radiation, the primary direction of photon diffusion is perpendicular to the orbital plane, and very little light emerges in directions close to the orbital plane.

The peak luminosity, spectrum, and lightcurve of eTDEs are therefore very different from those of ordinary TDEs, which are mostly observed in the optical with a peak luminosity lower by 1 order of magnitude, a rise time of order a month, and a postpeak luminosity falling as a steep power law in time. Although eTDEs' expected spectral shape in the X-ray band resembles that of ordinary TDEs (i.e., thermal with $T \sim 10^6$ K), the X-ray lightcurves of ordinary TDEs are qualitatively similar to those seen in the optical band (Auchettl et al. 2017; van Velzen et al. 2019; Jonker et al. 2020), rising comparatively gradually and then declining, rather than the extremely rapid rise to a plateau expected in eTDEs. Even more tellingly, the observed X-ray luminosities of ordinary TDEs ($\sim 10^{42}$–10^{43} erg s^{-1}: Auchettl et al. 2017) are much lower than the Eddington-limited luminosities we predict for eTDEs.[6]

4.2. Total Radiated Energy

Within the duration of our simulation, the luminosity estimated using the local cooling time sums to a total energy $\sim 2 \times 10^{48}(M_\star/M_\odot)$ erg. To estimate the radiated energy at later times, we first note that the total energy available is $\sim \eta_{\rm diss}\Delta M c^2$, where $\eta_{\rm diss}$ is the energy per unit mass acquired by the radiating debris from dissipative processes and ΔM is the amount of remaining bound mass in the hot compact settling flow. From shocks in this flow taking place at $\sim 50 r_{\rm g}$, $\eta_{\rm diss} \simeq 0.02$. The total bound mass is $\Delta M/M_\odot \simeq 0.15 M_\odot$, suggesting the total amount of energy radiated during the event might rise to $\sim 5 \times 10^{51}$ erg or more. Radiated at the Eddington luminosity, the luminosity we

have estimated at the end of our simulation, such a flare would last $\sim 1 (M_\star/1 M_\odot)(M_{\rm BH}/10^6 M_\odot)^{-1}$ yr.

4.3. Radio Flare

The interaction of the expanding ejecta with the surrounding gas should produce a radio flare (Krolik et al. 2016; Yalinewich et al. 2019; Matsumoto & Piran 2021). As discussed in the TDE context by Krolik et al. (2016), electron acceleration at the shock driven by the ejecta leads to synchrotron emission whose peak flux depends on the ejecta velocity as $F_\nu \propto f_A^{2/7} f_V^{5/7} v^{\frac{58-19k}{14}}$, where we assume the energy distribution of the emitting electrons is $\propto E_e^{-3}$, as is typical for Newtonian shocks. We further assume that the external density declines with distance $\propto r^{-k}$. The factors f_A and f_V describe the area and volume of the emitting region as compared with those of a spherical outflow (Barniol Duran et al. 2013). Because eTDEs have both unbound material with larger velocity and larger covering factors f_A and f_V, their characteristic radio signal should be larger by 1 order of magnitude compared to that of an ordinary TDE with the same external density. This stronger radio flare could help identifying eTDEs in addition to their strong earlier X-ray signature.

Initially the peak radio flux varies with time $\propto t^{19(2-k)/14}$ (Krolik et al. 2016). For a gradually declining density profile, like in the Milky Way (where $k \approx 1$), the radio luminosity increases with time. For steeper density profiles, like those observed in most TDE hosts, which generally have $k \approx 2$ (Matsumoto & Piran 2021), the flux is roughly constant. In either case the peak frequency decreases with time until eventually it drops significantly below 1 GHz and the source becomes undetectable. Overall, as a significant fraction of the unbound material moves at $\gtrsim 20{,}000$ km s^{-1} (see Section 3.2), which is much faster than a regular TDE, the radio signal should be brighter by about a factor of ~ 10 and longer by a factor of ~ 3 than the radio emission of ordinary (unjetted) TDEs.

4.4. Rate

For a fixed stellar distribution function that varies little across the loss cone, the rate of events having a pericenter less than r_p (measured in units of r_g) is $\propto L^2(r_p)$, which is $2r_p^2/(r_p - 2)$ in Schwarzschild spacetime. To illustrate how the relative rates of different varieties of TDEs depend on $M_{\rm BH}$, we show in the top panel of Figure 4 L^2 for partial TDEs, common full TDEs, circularized TDEs, eTDEs and direct capture events[7] and in the bottom panel the cross sections of the different varieties of observable full disruption events relative to their total. When the BH mass is relatively small ($10^6 M_\odot$), the rate of eTDEs is only $\simeq 6\%$ of all observable events (i.e., excluding direct captures). This fraction is, nonetheless, only about a factor of 3 smaller than that of circularized events for this BH mass. However, as $M_{\rm BH}$ increases, these extreme events become a much larger fraction of all those displaying observable signals: for $M_{\rm BH} \gtrsim 10^7 M_\odot$, they are $\gtrsim 40\%$ of all observable TDEs, becoming the majority for $M_{\rm BH} \gtrsim (2$–$4) \times 10^7 M_\odot$ (depending on the stellar mass). If we apply these relative rates to the observationally calibrated TDE rate estimated by Stone & Metzger (2016), the rate of

---

[6] There are three cases presented in Auchettl et al. (2017) with higher X-ray luminosities, but their nature is uncertain because each has only a single observation.

[7] Following Krolik et al. (2020), we define circularized TDEs to be events with strong enough relativistic apsidal precession for debris to circularize rapidly.
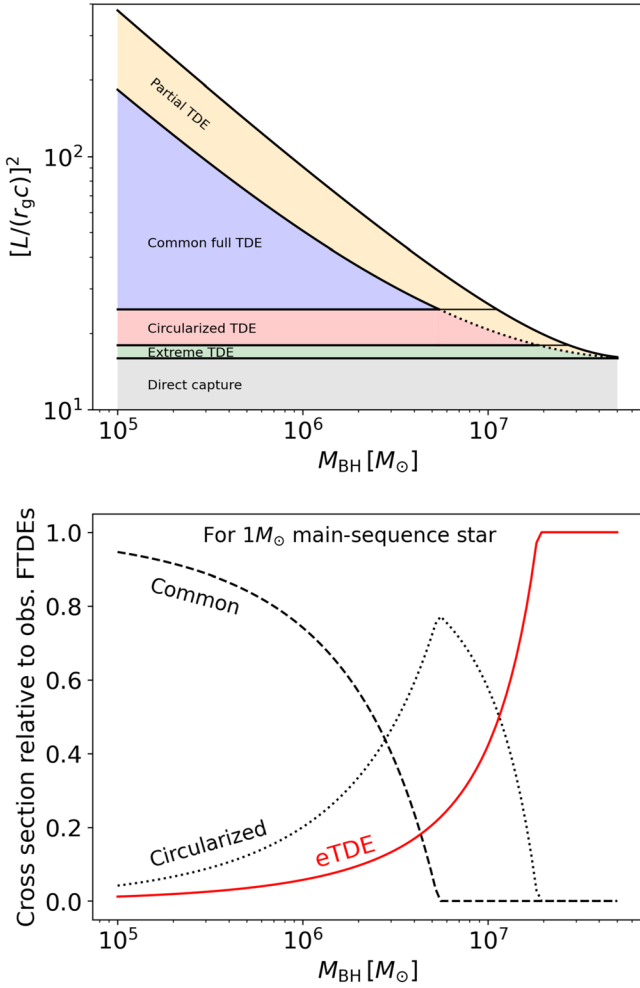
Figure 4. (Top) Regions in parameter space for five kinds of disruption events: partial TDE (orange), common full TDE (blue), circularized TDE (red), and direct capture (gray, $r_p < 4_g$). We define partial TDEs as events where the star loses more than 10% of its mass at the first pericenter passage. This plot is an extended version of Figure 3 in Krolik et al. (2020). (Bottom) The cross section as a function of M_{BH} for each class of observable full disruption events, i.e., common (dashed black), circularized (dotted black), extreme (solid red), in units of the total disruption cross section for a $1\,M_\odot$ main-sequence star.

eTDEs as a function of M_{BH} peaks at $M_{BH} \simeq 2 \times 10^7\,M_\odot$, where the rate is $\approx 6 \times 10^{-5}\,\mathrm{yr}^{-1}$ per galaxy.

5. Summary and Conclusion

In this paper, we examined the long-term evolution of debris produced in extremely relativistic tidal disruption events of a realistic main-sequence $1\,M_\odot$ star by a $10^6\,M_\odot$ SMBH using fully relativistic hydrodynamics simulations with realistic initial conditions. We considered several different pericenter distances ranging from $r_p \simeq 4.03$–$7 r_g$. Strikingly, extremely strong apsidal precession, which occurs only for $r_p \lesssim 6 r_g$, leads to a debris evolution qualitatively different from that for ordinary disruption events. The debris undergoes four different phases: it is elongated to form a crescent that stretches to form a spiral wrapping around the SMBH. The spiral expands outward, and then its several windings merge into a ring that continues to advance outwards. The bound material of the ring eventually falls back toward the SMBH and forms a roughly spherical accretion flow near the SMBH. The resulting hot ($\sim(1$–$2) \times 10^6$ K) accretion flow is the main source of

radiation. Our detailed analysis indicates that the luminosity rises on a timescale ($\sim$3 hr for $M_{BH} \sim 10^6 M_\odot$) much shorter than the flare duration ($\sim 1\,(M_{BH}/10^6 M_\odot)^{-1}$ yr). For most of its duration, the flare should maintain approximately the Eddington luminosity of the SMBH, but then decline as a shallow power law when the continued infall cannot sustain that luminosity.

These events should be detectable by eROSITA as X-ray events that are accompanied by weak or no optical signal. The interaction of the high velocity ($\gtrsim$20,000 km s^{-1}) escaping unbound material with the surrounding matter should lead to a powerful radio flare (Krolik et al. 2016; Yalinewich et al. 2019; Matsumoto & Piran 2021) that follows these events by a few weeks.

Thus, even though they are genuine tidal disruptions, their lightcurves and spectra are very different from classical expectations; consequently, matching the classical expectations should not be an absolute prerequisite for classification as a TDE. Although these events are probably rare for lower-mass SMBHs (i.e., $M_{BH} \lesssim 10^6 M_\odot$), they should be the dominant tidal disruption events yielding flares for $M_{BH} \gtrsim 3 \times 10^7 M_\odot$. Moreover, any such event in an SMBH of this mass would be exceptionally luminous because $L_E \simeq 4.5 \times 10^{45}(M_{BH}/3 \times 10^7 M_\odot)$ erg s^{-1}.

Appendix A
Numerical Grid

In the simulations with a spherical grid, we adopt modified spherical coordinates in Schwarzschild spacetime: the modified spherical coordinate variables (r', θ', ϕ') are related to ordinary spherical coordinates (r, θ, ϕ) by

$$r = e^{r'}, \qquad (A1)$$

$$\theta = \theta_0(\tanh[b(\theta' - a)] + \tanh[b(\theta' + a)]) + 0.5\pi, \quad (A2)$$

$$\phi = \phi'. \qquad (A3)$$

Here, $\theta_0 = -(0.5\pi - \theta_c)/[\tanh(b(-0.5 - a)) + \tanh(b(-0.5 + a))]$. The angle θ_c is the opening angle of the polar cutout, and a and b are a set of tuning parameters that determine the vertical structure, which are given within $0.32 \leqslant a \leqslant 0.35$ and $9.8 \leqslant b \leqslant 10$. These modified coordinates allow us to place the grid cells where they are most needed in the simulation domain. The radial grid cells have constant $\Delta r/r$ and the vertical cells are more concentrated toward the midplane. To minimize the computational cost, we flexibly adjust the domain extent in θ and r. During the grid transition, we adjust the number of cells to ensure that there are more than 15–20 cells per scale height in r, θ, and ϕ.

The boundary conditions are outflow for the r and θ boundaries and periodic for the ϕ boundary. The Courant number is 0.3.

Appendix B
Luminosity Estimate

Because our simulations do not include time-dependent radiation transfer, we estimate the luminosity based on the local cooling time. Here, we define the local cooling time as $t_{\rm cool} = h_\rho \tau (1 + u_{\rm gas}/u_{\rm rad})/c$ where h_ρ is the density scale height along the θ direction, τ is the optical depth integrated along θ coordinate curves from the polar angle cutout to the individual cells and $u_{\rm gas}$ ($u_{\rm rad}$) is the local gas thermal (radiation) energy contained within the cell. The opacity is found in terms of ρ and T using an OPAL opacity table for solar metallicity (Iglesias & Rogers 1996). Figure 5 shows the shape of the photosphere in the $r-z$ plane at $\phi = 0$ at four different times.

At early evolutionary stages ($t \lesssim$ a few hours, where t is the time since pericenter passage), the gas is packed into dense spirals that then merge into an expanding ring. Because the cooling time is very long ($t_{\rm cool} \gtrsim$ a few months), the evolution is nearly adiabatic and we expect little energy is radiated.

At later stages, bound debris falls back toward the BH, shocks against itself, and forms an accretion flow, while the unbound ring expands outward. At the end of the simulation for our fiducial model ($t \simeq 0.6$ days), $t_{\rm cool}$ very near the SMBH is only ~ 1 hr, but increases gradually and monotonically outward, reaching a few months in the expanding ring. From $t \sim 10^4$ s onward, the distance at which $t_{\rm cool} = t$ remains constant at $\simeq 70 r_{\rm g}$.

The fact that the dividing line between regions where $t_{\rm cool} < t$ and where $t_{\rm cool} > t$ stays roughly fixed in place allows us to split the entire system into three regions depending on $t_{\rm cool}/t$: (1) the inner region of the hot accretion flow ($r \lesssim 70 r_{\rm g}$), where $t_{\rm cool} \lesssim t$; (2) the rest of the hot accretion flow, where $t_{\rm cool} \gtrsim t$; and (3) the expanding ring, which has the longest

cooling time (~ 0.1–1 yr). This distinction is important because radiation transfer can reach a steady state only when the photon diffusion time (here essentially $t_{\rm cool}$) is comparable to or shorter than the evolution time. Put another way, the probability distribution function for the emergence of photons from an optically thick region cuts off much more sharply than linearly for times longer than the photon diffusion time; hence estimating the luminosity by the ratio of thermal energy to cooling time is valid only for $t_{\rm cool} \lesssim t$; when the cooling time is longer, using this ratio leads to a severe overestimate of the luminosity.

We therefore begin our estimate of the luminosity with region (1), where our methods are most secure.

We estimate its total luminosity by integrating the local emissivity of the individual cells with respect to polar angle within the thermalization photosphere at $\sqrt{\tau_{\rm T} \tau_{\rm ff}} \simeq 1$. Here, $\tau_{\rm T}$ ($\tau_{\rm ff}$) is the Thomson (absorption) optical depth integrated inwards from the θ boundary along the θ direction. The luminosity from cells in each column above the midplane along the polar axis is calculated as

$$l_{\rm up}(r, \phi) = \int_{\pi/2}^{\theta_{\rm ph,up}} aT^4 t_{\rm cool}^{-1} r \sin\theta d\theta, \qquad (B1)$$

where a is the radiation constant and $\theta_{\rm ph,up}$ is the polar angle of the cell closest to the photosphere for given r and ϕ above the midplane. l below the midplane ($l_{\rm down}$) is calculated similarly by integrating from $\pi/2$ to $\theta_{\rm ph,down}$. To find the total luminosity, we integrate l for each (r, ϕ) on the grid with $t_{\rm cool} < t$ gives the total luminosity L,

$$L = \frac{1}{2} \int_0^{2\pi} \int_{r=R_{\rm in}}^{r(t_{\rm cool}<t)} (l_{\rm up} + l_{\rm down}) r dr d\phi, \qquad (B2)$$

where $R_{\rm in}$ is the radius of the inner radial cutout and $\theta_{\rm ph,up}(\theta_{\rm ph,down})$ is the polar angle of the photosphere above (below) the midplane. The effective temperature at each
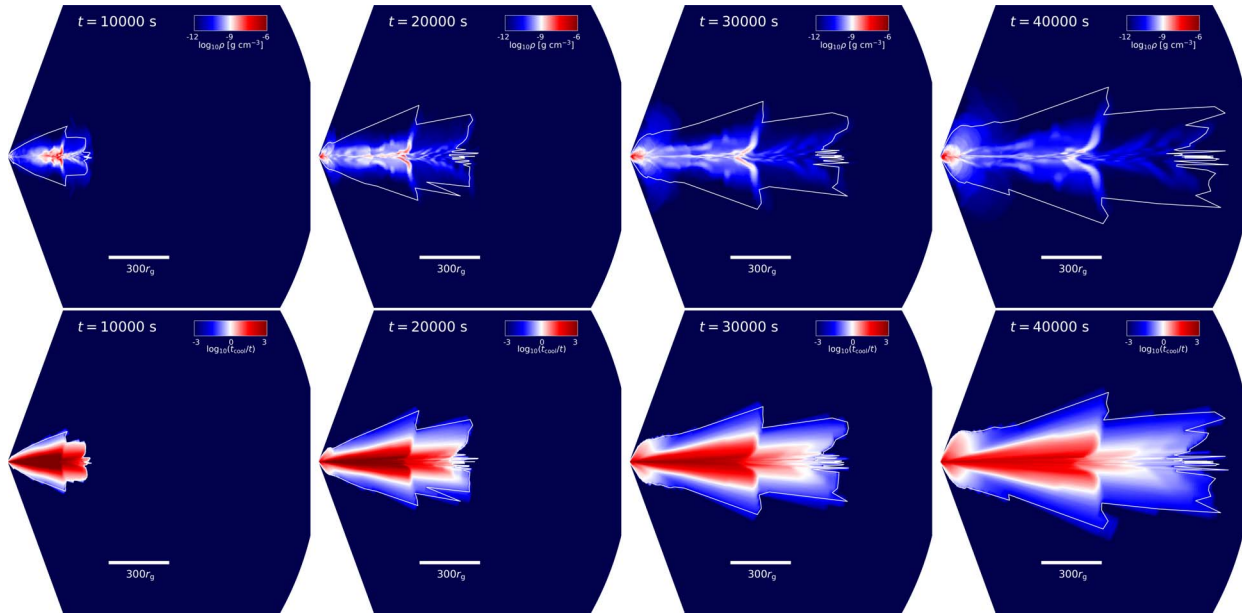

Figure 5. The distribution of the density (top) and the ratio of the cooling time to the evolution time (bottom) in the $r-z$ plane at $\phi = 0$ at $t \simeq 10,000, 20,000, 30,000,$ 40,000 s. The location of the thermalization photosphere as seen by a distant observer is plotted using a white line. We define the thermalization optical depth as $\sqrt{\tau_{\rm T} \tau_{\rm ff}}$, for $\tau_{\rm T}$ ($\tau_{\rm ff}$) the Thomson (absorption) optical depths integrated radially inwards from the outer boundary. The prominent break in structure roughly halfway out in the debris corresponds to the density peak of the expanding ring.
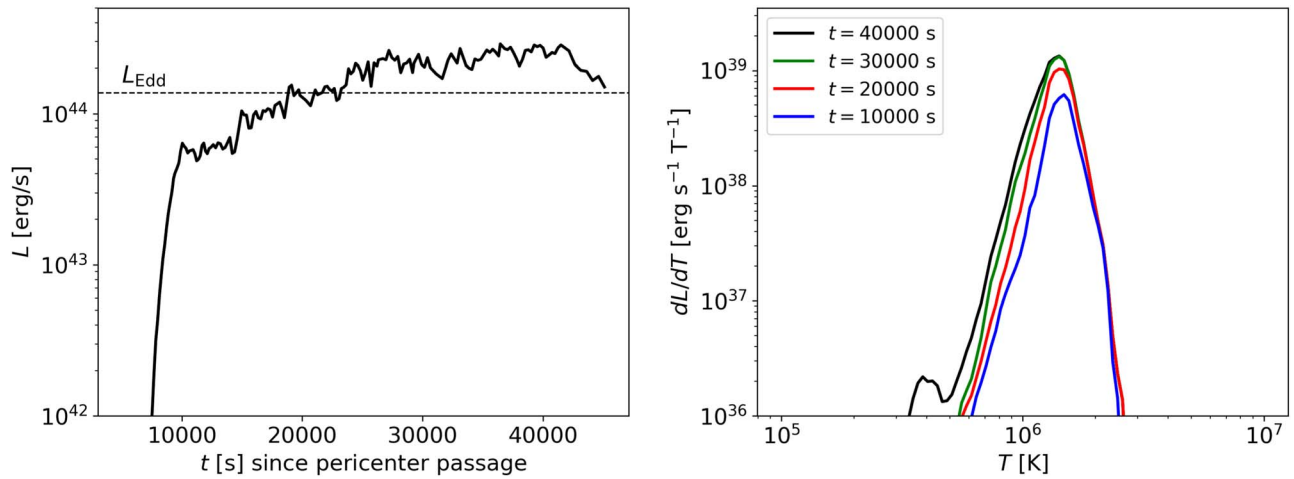
Figure 6. The luminosity estimated using Equation (B2) as a function of time (left) and the distribution of the temperature dL/dT at a few different times (right). The horizontal dashed line in the left panel indicates the Eddington limit for $M_{\rm BH} = 10^6 \, M_\odot$.

individual cell near the photosphere is then calculated as $T = (l/\sigma)^{1/4}$, where σ is the Stefan–Boltzmann constant. We find that after the accretion flow forms ($t \sim 10^4$ s), the total luminosity remain roughly constant in time at $\sim (2\text{–}3) \times 10^{44}$ erg s^{-1}, which is roughly the Eddington luminosity for our $10^6 M_\odot$ SMBH, as demonstrated in the left panel of Figure 6. And the temperature remains at $T \simeq (1\text{–}2) \times 10^6$ K (see the right panel of Figure 6). That its luminosity is roughly Eddington should not be surprising; dimensional analysis alone shows that the Eddington luminosity is the characteristic cooling rate of any plasma whose opacity is close to Thomson and is supported by radiation pressure against gravity (Krolik 2010).

Estimating the luminosity for regions (2) and (3) is more difficult because its radiation transport is not in a steady state. The flux reaching the surface may not be well estimated by $U_{\rm rad}/t_{\rm cool}$; in addition, a diffusion time longer than the dynamical time means that the radiation pressure can do work on the matter, transforming photon energy in gas kinetic energy, or vice versa. Qualitatively, we might expect that at later times in region (2), the gas is likely to fall inward by a factor of several; the compression should increase its total energy by the same factor. At the same time, however, its cooling time should increase by the same length scale ratio because the gas's scale length, but not its optical depth, changes. On this basis, we will crudely estimate its contribution to the luminosity from $U_{\rm rad}/t_{\rm cool}$ at the end of the simulation; this yields $\sim 3 \times 10^{43}$ erg s^{-1}. It might therefore be less luminous than the inner region by a factor of a few.

In region (3), the radiation escape time is a great deal larger than the simulated evolution time. Because this region moves outward, the radiation energy it carries is reduced by the work done in adiabatic expansion. How rapidly this occurs can be estimated by examining the time scaling of this region as revealed by the simulation. Both the cooling time and the total radiation energy contained within the expanding ring follow simple power laws, $t_{\rm cool} \propto t^{-0.8}$ and $U_{\rm rad} \propto t^{-0.4}$. Extrapolating these power laws out to the time at which $t_{\rm cool} = t$ allows us to predict the luminosity when the photons from this region actually can escape. At this time ($\simeq 5$ days), we find that the radiation energy has diminished to $\simeq 3.4 \times 10^{48}$ erg. This

implies a luminosity from the expanding ring of $\simeq 7 \times 10^{42}$ erg s^{-1} during a period of several days around $t \simeq 5$ days. This is rather less than the the emission from region (2) at this stage.

ORCID iDs

Taeho Ryu ⓘ https://orcid.org/0000-0003-2012-5217
Julian Krolik ⓘ https://orcid.org/0000-0002-2995-7717
Tsvi Piran ⓘ https://orcid.org/0000-0002-7964-5420

References

Auchettl, K., Guillochon, J., & Ramirez-Ruiz, E. 2017, ApJ, 838, 149
Barniol Duran, R., Nakar, E., & Piran, T. 2013, ApJ, 772, 78
Batra, G., Lu, W., Bonnerot, C., & Phinney, E. S. 2021, arXiv:2112.03918
Carter, B., & Luminet, J. P. 1983, A&A, 121, 97
Cheng, R. M., & Bogdanović, T. 2014, PhRvD, 90, 064020
Darbha, S., Coughlin, E. R., Kasen, D., & Nixon, C. 2019, MNRAS, 488, 5267
Evans, C., Laguna, P., & Eracleous, M. 2015, ApJL, 805, L19
Gafton, E., & Rosswog, S. 2019, MNRAS, 487, 4790
Gezari, S. 2021, ARA&A, 59, 21
Goicovic, F. G., Springel, V., Ohlmann, S. T., & Pakmor, R. 2019, MNRAS, 487, 981
Guillochon, J., & Ramirez-Ruiz, E. 2013, ApJ, 767, 25
Halpern, J. P., Gezari, S., & Komossa, S. 2004, ApJ, 604, 572
Hung, T., Gezari, S., Blagorodnova, N., et al. 2017, ApJ, 842, 29
Hunter, J. D. 2007, CSE, 9, 90
Iglesias, C. A., & Rogers, F. J. 1996, ApJ, 464, 943
Jonker, P. G., Stone, N. C., Generozov, A., van Velzen, S., & Metzger, B. 2020, ApJ, 889, 166
Kobayashi, S., Laguna, P., Phinney, E. S., & Mészáros, P. 2004, ApJ, 615, 855
Komossa, S., & Bade, N. 1999, A&A, 343, 775
Kormendy, J., & Ho, L. C. 2013, ARA&A, 51, 511
Krolik, J., Piran, T., & Ryu, T. 2020, ApJ, 904, 68
Krolik, J., Piran, T., Svirski, G., & Cheng, R. M. 2016, ApJ, 827, 127
Krolik, J. H. 2010, ApJ, 709, 774
Lacy, J. H., Townes, C. H., & Hollenbach, D. J. 1982, ApJ, 262, 120
Laguna, P., Miller, W. A., Zurek, W. H., & Davies, M. B. 1993, ApJL, 410, L83
Lodato, G., King, A. R., & Pringle, J. E. 2009, MNRAS, 392, 332
Lu, W., & Bonnerot, C. 2020, MNRAS, 492, 686
Matsumoto, T., & Piran, T. 2021, MNRAS, 507, 4196
Noble, S. C., Krolik, J. H., & Hawley, J. F. 2009, ApJ, 692, 411
Paxton, B., Bildsten, L., Dotter, A., et al. 2011, ApJ Supp., 192, 3
Phinney, E. S. 1989, in IAU Symp.136, The Center of the Galaxy, ed. M. Morris (Dordrecht: Kluwer), 543
Piran, T., Svirski, G., Krolik, J., Cheng, R. M., & Shiokawa, H. 2015, ApJ, 806, 164
Rees, M. J. 1988, Nat., 333, 523

Ryu, T., Krolik, J., Piran, T., & Noble, S. C. 2020a, ApJ, 904, 98
Ryu, T., Krolik, J., Piran, T., & Noble, S. C. 2020b, ApJ, 904, 99
Shiokawa, H., Krolik, J. H., Cheng, R. M., Piran, T., & Noble, S. C. 2015, ApJ, 804, 85
Steinberg, E., & Stone, N. C. 2022, arXiv:2206.10641
Stone, N. C., & Metzger, B. D. 2016, MNRAS, 455, 859

Svirski, G., Piran, T., & Krolik, J. 2017, MNRAS, 467, 1426
Tejeda, E., Gafton, E., Rosswog, S., & Miller, J. C. 2017, MNRAS, 469, 4483
van Velzen, S., Gezari, S., Hammerstein, E., et al. 2021, ApJ, 908, 4
van Velzen, S., Stone, N. C., Metzger, B. D., et al. 2019, ApJ, 878, 82
Yalinewich, A., Steinberg, E., Piran, T., & Krolik, J. H. 2019, MNRAS, 487, 4083